Proceedings of the 3rd International Conference on Functional Materials and Civil Engineering
DOI: 10.54254/2755-2721/2025.24578

Study on Properties Optimization and Advanced Preparation Techniques of Alumina Ceramic Electronic Substrates

Libohang Zhang[1]*, Tiankuo He[1], Ye Liu[1]

[1]*Northwestern Polytechnical University, Xian, China*
**Corresponding Author. Email: 44120388@mail.nwpu.edu.cn*

Abstract. Alumina (Al_2O_3) ceramics have become indispensable materials in the field of electronic substrates due to their excellent thermal conductivity, high insulation, and mechanical stability. This study systematically investigates the atomic bonding, crystal structure, and phase transformation behaviors of Al_2O_3 under various synthesis and sintering conditions. Emphasis is placed on the correlation between phase diagrams and material performance, particularly in relation to impurity control and sintering aids such as MgO. The findings provide a theoretical and practical basis for optimizing the preparation of high-purity α-Al_2O_3 substrates to meet the stringent requirements of modern electronic packaging.

Keywords: Alumina ceramics, Electronic substrates, Phase diagram, Sintering, Dielectric performance

1. Introduction

1.1. Introduction and background

With many outstanding properties including high hardness, wear resistance, excellent insulation and chemical stability, ceramic materials have been widely applied in recent years. Among them, alumina (Al_2O_3) ceramic substrates play a crucial role in electronic packaging due to high hardness, high thermal conductivity and high insulation, and are particularly suitable for packaging integrated circuits and optoelectronic devices [1]. This report mainly discusses the entire process of the structure, reaction, preparation and characterization of the α-Al_2O_3 ceramics, and looks forward to their application as substrates in electronic packaging [2].

1.2. Key performance and applications

The excellent properties of alumina ceramic substrates make them indispensable in the electronic packaging industry. Their high insulating properties ensure reliable electrical isolation in components such as MEMS sensors and integrated circuits. Alumina has a thermal conductivity of approximately 25 W/mK, which allows heat generated by high-power devices to dissipate efficiently and prevents high-temperature failure [3]. The high mechanical strength of alumina ceramics enhances the durability of electronic components in harsh environments, and their high chemical stability ensures the components' resistance to corrosion and oxidation, guaranteeing their long-term operation. Furthermore, the alumina ceramic substrate doped with transition metal oxides (e.g., Fe_2O_3, CoO, MnO_2) has excellent light-blocking ability, which is crucial for reducing the influence of stray light on photoreceptors [4]. These excellent properties make alumina ceramics an ideal solution for establishing advanced electronic packaging systems [5].

2. Structure

2.1. Atomic bonding

Alumina contains both covalent bonds and ionic bonds. This bonding typically occurs between oxygen and aluminum ions. At the same time, we know that the electronegativity of aluminum is 1.61, while that of oxygen is 3.34. This significant difference in electronegativity also results in a higher strength of ionic bonds.Some covalent bonding comes from orbital hybridization. Some covalent bonding also comes from local coordination environments. This hybrid bonding is the basis of alumina stability.

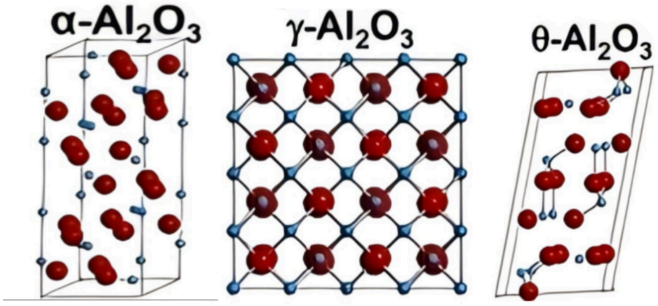

Figure 1: Common crystal structures of aluminium oxide [6]

In figure1,this bonding interaction gives alumina a high melting point, greater than 2000°C, a high Young's modulus and excellent chemical inertness. These properties are critical in electronic substrate applications. Strong bonding results in minimal structural degradation of alumina during high temperature operation. In addition, with a large bandgap of about 8.7 eV, α-Al_2O_3 has high insulation and well suitability for supporting electronic components to prevent parasitic current leakage.

However, not all alumina phases have the same bonding network. In γ-Al_2O_3, the defective spinel structure introduces disordered aluminum ions to occupy sites and vacancies. This may reduce the dielectric properties. One relevant study showed that, the band gap of γ-Al_2O_3 collapses from about 4 eV to zero under the action of an external electric field and transforms into a metal-like behavior. This suggests that under electrical stress, the substable phase may introduce unpredictability in device performance under electrical stress.

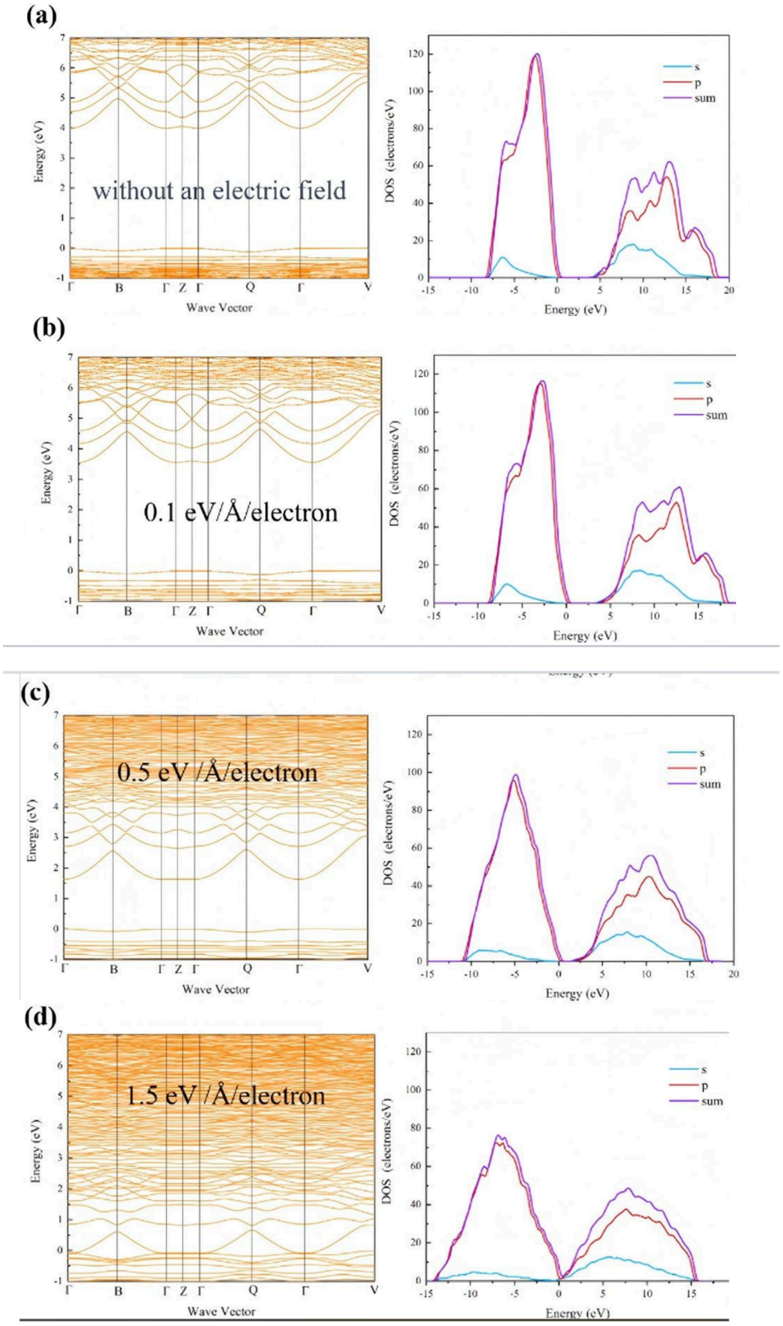

Figure 2: Energy band structure and density of states (projected density of states, PDOS: blue line indicates s-orbital contribution, red line indicates p-orbital contribution, and purple line indicates the total contribution of s and p orbitals) of γ-Al_2O_3 under different external electric fields. (a) Band gap width of 3.996 eV in the absence of an external electric field; (b) band gap width of 3.559 eV with an external electric field of 0.1 eV/Å/electron applied along the z-axis; (c) band gap width of 1.627 eV with an external electric field of 0.5 eV/Å/electron applied along the z-axis; and (d) band gap width of 0 eV with an external electric field of 1.5 eV/Å/electron applied along the z-axis [7]

From Figure 2,for amorphous AlOx films synthesized by atomic layer deposition (ALD), local bonding is highly dependent on processing conditions. Synchrotron X-ray and Pair Distribution Function (PDF) analysis show Al–O bond lengths clustering around 1.8 Å, with the coordination number varying based on film thickness. This implies that nanoscale films do not have a single, repeatable structure, but instead contain a spectrum of local environments.

From the above, it can be seen that understanding these bonding changes is extremely important. In practical applications, if the film is thin, then the atomic coordination will be less, which will result in poor mechanical properties and low thermal conductivity. This will directly affect the quality of the aluminum oxide substrate in some small electronic devices [8].

2.2. Crystal structure

Among the polymorphs of Al_2O_3, α-Al_2O_3 is the most stable. It is widely used in electronic substrates. It has a corundum-type hexagonal structure, with space group R-3c. The lattice constants are a = 4.76 Å and c = 12.99 Å. In this structure, Al^{3+} ions fill about two-thirds of the octahedral sites. The atoms pack tightly in a symmetric way. This reduces ion movement and improves thermal conductivity. The density of α-Al_2O_3 is approximately 3.98 g/cm^3, and its thermal conductivity ranges from 25 to 35 W/m·K at room temperature, depending on purity and microstructure.

α -Al_2O_3 is a good insulator. It also conducts heat well. It blocks physical contact and electrical interference between components. Its strong structure allows precise processing with little deformation [9].

γ -Al_2O_3 is different. It is a metastable phase. It has a defective spinel-like structure. The space group is Fd$\bar{3}$m. The Al^{3+} ions are located in tetrahedral and octahedral positions. Many positions are empty. These vacancies disturb the structure. They increase phonon scattering and reduce thermal conductivity. The density of γ-Al_2O_3 is relatively low, approximately 3.6 grams per cubic centimeter, because its structure is not tightly packed and there are vacancies. Moreover, its thermal conductivity is also relatively low, typically less than 10 watts per meter per kelvin, and the specific value mainly depends on the porosity [10].

Amorphous Al_2O_3 forms at low temperature. It comes from atomic layer deposition (ALD). It has no long-range order, but local Al–O bonds still exist. Pair Distribution Function analysis shows Al–O bond lengths are close to those in crystals. As the film becomes thicker, more Al atoms shift to octahedral coordination. This change may come from stress release and higher density during growth. Amorphous Al_2O_3 typically has the lowest thermal conductivity among the three, often below 2 W/m·K, due to its disordered structure and high phonon scattering. Its density is usually around 3.0–3.4 g/cm^3 [11].

Recent studies used machine learning and DFT to study γ-Al_2O_3. The results showed that its structure is not the same as the ideal spinel. Octahedral vacancies reduce the system's energy. These vacancies cause local distortion and help the structure stay stable in some conditions.

γ-Al_2O_3 does not have a single fixed structure. Simple crystal models often overlook this situation. For instance, some γ-Al_2O_3 samples are formed during rapid cooling or low-temperature growth processes, and such samples often exhibit disorder . Therefore, the underlying model may not match the actual material, and we need more advanced tools to characterize structures with defects or irregular shapes [12].

3. Phase

3.1. Select representative binary and ternary phase diagrams

For alumina in electronic substrates, if we consider a binary phase diagram, according to the research by Wang et al., the impurity that is most easily introduced during sintering is SiO_2 [13]

.Therefore, in the selection of a typical binary phase diagram, we have adopted the Al_2O_3-SiO_2 binary phase diagram, as shown in the figure below.

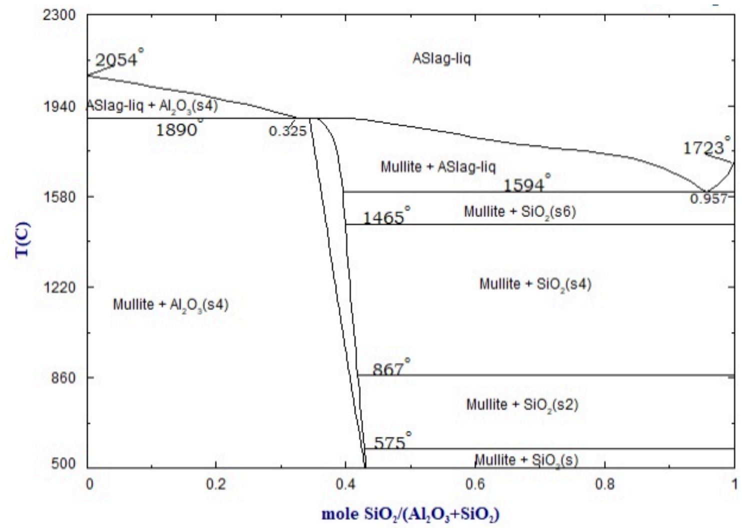

Figure 3: binary phase diagrams of Al_2O_3-SiO_2

Similarly, when considering a ternary phase diagram in figure 3, in the sintering of Al_2O_3, SiO_2 remains the primary impurity. Additionally, according to the research by Kang et al., we introduce the sintering aid MgO [14]. So, there is forming a ternary phase diagram system. Figure 4 is the Al_2O_3-SiO_2-MgO ternary phase diagram.

In connection with our task1, the high purity α-Al_2O_3 shown in the diagram is essential for insulation (ε_r=9.4) and mechanical strength (300-400 MPa). At the same time, reducing the sintering temperature to 1350°C instead of the traditional 1600°C can reduce energy consumption and CO_2 emissions [15].

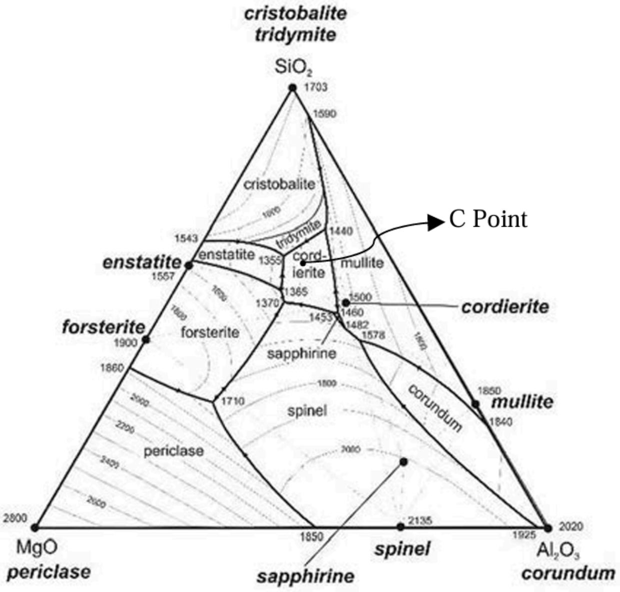

Figure 4: Al_2O_3-SiO_2-MgO ternary phase diagram [16]

3.2. Phase transformations

In the Al_2O_3-SiO_2-MgO ternary phase diagrams, to show the specific phase change of Al_2O_3, we reference the paper by Martin and selected a composition of 97% Al_2O_3, 2% MgO, and 1% SiO_2 [17]. For the phase transformations upon cooling from the molten state (>2020°C), a single liquid phase (L) exists [18]. For the primary phase precipitation (~2020°C), α-Al_2O_3 begins to precipitate. From 2020-1600°C the remaining liquid phase cooling, The liquid phase becomes enriched in MgO and SiO_2(in figure 5), and a binary eutectic reaction may occur (L → α-Al_2O_3 + Spinel ($MgAl_2O_4$)). Below 1600°C in the low-temperature region, a small amount of glass phase (enriched in SiO_2) may form, but it is suppressed by MgO (as a sintering aid).

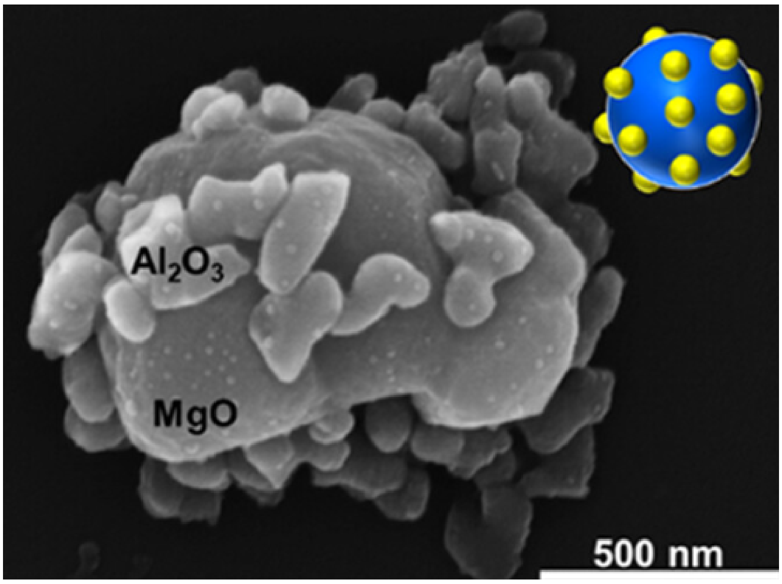

Figure 5: Al_2O_3 phase transition precipitation at low temperatures

According to theoretical predictions, the phase diagram shows that only α-Al_2O_3 and trace Spinel exist at low temperatures .

The actual deviation is mainly affected by two aspects, the first one is due to non-equilibrium cooling, that is, laser melting or rapid sintering may cause metastable phase (such as θ-Al_2O_3) residual. Second, due to the influence of impurities, trace SiO2 may be locally enriched to form a glass phase or react with Al_2O_3 to form mullite ($3Al_2O_3 \cdot 2SiO_2$). Experiments show that adding 2% MgO can inhibit the glass transition tendency of SiO_2, but local component fluctuations may lead to non-equilibrium phase [19].

The external factors are mainly affected by the heat treatment atmosphere. Under the oxidizing atmosphere (air), the oxygen vacancy can be inhibited and the stability of α-Al_2O_3 can be maintained, which is beneficial to the subsequent production. However, in a reducing atmosphere (H_2), SiO_2 may be reduced to Si, leading to the introduction of more impurities.

For the first-order phase transition, α-Al_2O_3 precipitates with latent heat release and causes volume effects leading to volume shrinkage (about 5%) [20]. Rapid cooling may lead to micro-cracks, and the cooling rate should be controlled (<5°C/min). According to the experiments of zhang et al., the volume of α→θ-Al_2O_3 phase transition changes by 2-3% [21]. For second-order phase transition, there is no volume mutation, but the solid solution of MgO may cause lattice distortion and affect the thermal conductivity [22].

There are three main in-situ characterization techniques to validate phase transitions. The first is high-temperature XRD, and the phase transition can be verified by real-time monitoring of the characteristic peaks (2θ=32.1°, 43.3°) and Spinel (2θ=36.8°) in alpha-Al_2O_3

The second method is SEM-EDX, which determines the uniformity of MgO and SiO_2 distribution by analysing the composition of the primary phase.

The last is Raman spectroscopy, through in-situ detection of trace glass phase, SiO_2 vibration peak wave number is 480 cm^{-1}.In figure 6 we can see the XRD pattern of the molten $3Al_2O_3{\cdot}2SiO_2$.

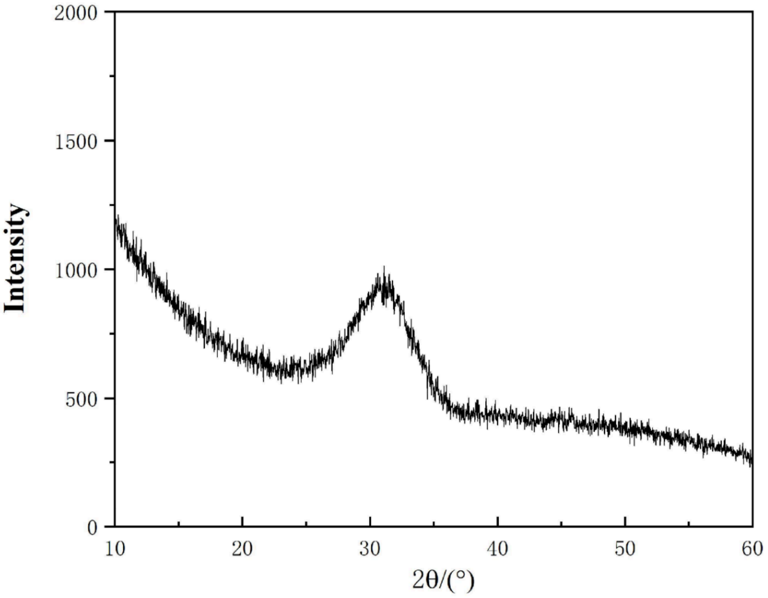

Figure 6: The XRD pattern of the molten $3Al_2O_3{\cdot}2SiO_2$ [23]

Through the above analysis of the phase diagram, the correlation between the performance mentioned above and the application of electronic substrates can be reflected in the following aspects. Firstly, high purity α-Al_2O_3 ensures that the dielectric constant can achieve insulation, and $\tan\delta<0.001$. Low loss can guarantee the long-term use of electronic substrates.

In the application of electronic substrates, an appropriate thermal conductivity is also a performance that we need to consider. The thermal conductivity of high-purity α-Al_2O_3 is 30 W/mK [24], which can meet the heat dissipation requirements of electronic devices.

Meanwhile, through the phase diagram, we can infer the reliability of high-purity α-Al_2O_3 as an electronic substrate. Through our binary phase diagram and ternary phase diagram, high-purity α-Al_2O_3 can avoid the glass phase and the unstable phase and reduce the risk of thermal stress cracking.

3.3. Interpretation

To determine the most suitable phase for the electronic substrate, we further analyse the binary phase diagram (Al_2O_3-SiO_2) respectively. Firstly, the tolerance limit for impurity SiO_2 is determined to be 1% [25]. In the phase selection of the electronic substrate, it is necessary to avoid the formation of mullite ($3Al_2O_3{\cdot}2SiO_2$) or glass phase. For instance, the phase diagram Fig3-3-1 shows that below 1600 ° C, the eutectic reaction between Al_2O_3 and SiO_2 leads to the formation of a glass phase, but the addition of MgO (2%) can inhibit this reaction.

Meanwhile, we can also further determine based on the ternary phase diagram (Al_2O_3-MgO-SiO_2) that the required component points are in the primary phase region of α-Al_2O_3, indicating that the high-purity α phase is the dominant phase, which can ensure the insulation and mechanical strength of the electronic substrate. Meanwhile, a trace amount of MgO promotes densification, while SiO_2 is confined in spinel ($MgAl_2O_4$) [26].

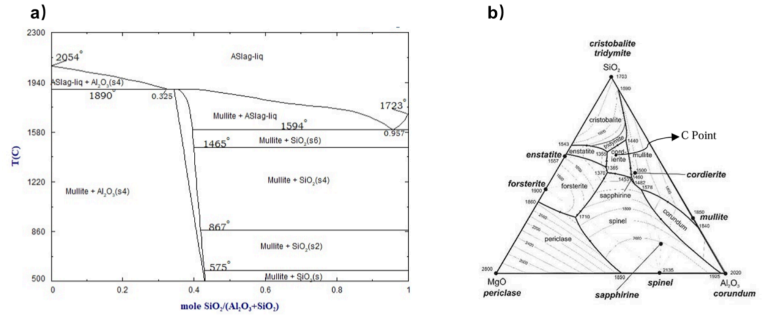

Figure 7: a) binary phase diagrams of Al_2O_3-SiO_2

b) Al_2O_3-SiO_2-MgO ternary phase diagram

However, when we determine the most suitable phase based on the phase diagram, it should be noted that the phase diagram is based on thermodynamic equilibrium conditions and does not take into account the non-equilibrium effects in the actual process, such as the residual θ-Al_2O_3 caused by rapid cooling mentioned by jack et al., which may need to be corrected in combination with other reference materials such as the kinetic model.

There is a significant relationship among the phase diagram, processing performance and the final application. Through the binary phase diagram of Al_2O_3-MgO, the liquid phase formation temperature can be reduced to 1600-1700℃ by adding 2% MgO [27]. Under this sintering capacity, densification (relative density >98%) is promoted, and abnormal grain growth is inhibited simultaneously. The interface compatibility of spinel (matching of thermal expansion coefficients) ensures the reliability of the final electronic substrate.

It should also be noted that the sintering temperature should be maintained above 1500 ℃. Although low-temperature sintering (1350 ℃) reduces energy consumption, it may lead to insufficient density, requiring an extended holding time, which in turn increases production costs .

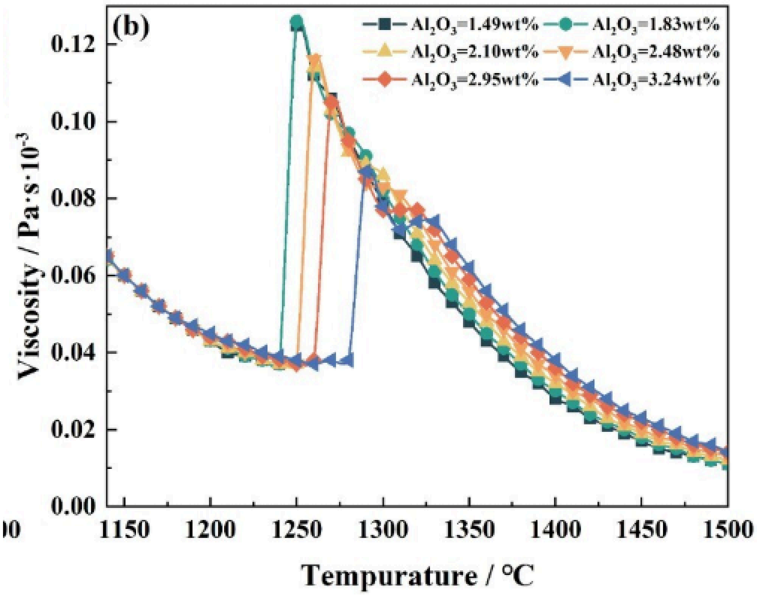

Figure 8: Effect of the Al_2O_3 viscosity at low temperature (above 1500°C) [28]

In an oxidizing atmosphere or an air atmosphere, the phase diagram predicts a low oxygen vacancy concentration. Based on the phase diagram, it can be judged that fewer vacancies are formed, reducing dielectric loss. This can meet the dielectric performance requirements of the final application. If in a reducing atmosphere of H_2, SiO_2 may be reduced to Si, introducing conductive defects [29].

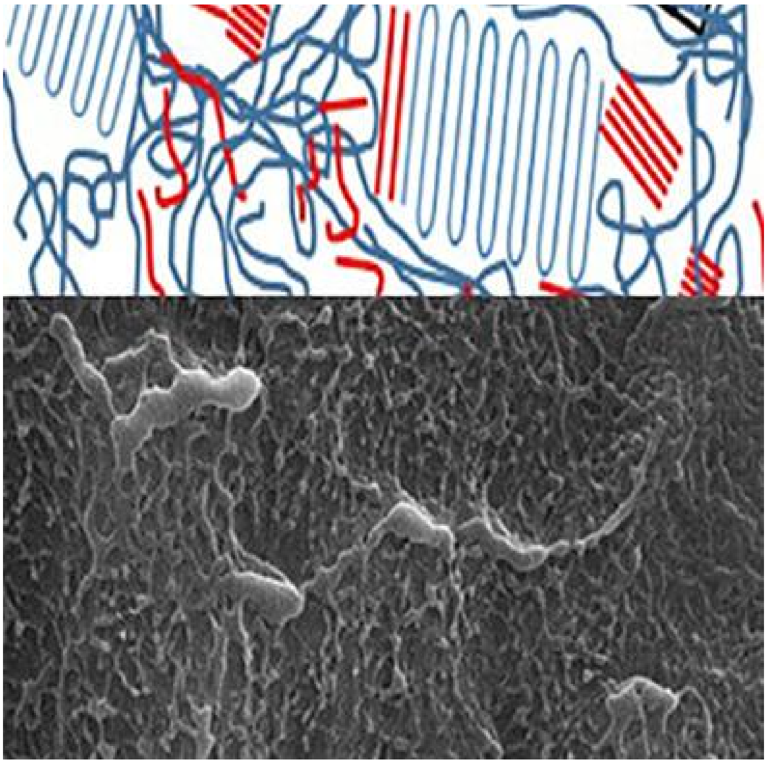

Figure 9: An enlarged MgO addition effect diagram [30]

When developing materials for electronic substrates, the material composition is timed, and the optimal addition amount of MgO(in figure 9) is determined to be 2% through the phase diagram to balance densification and impurity control. For instance, according to the research by Chamasemani et al., an excessive amount of MgO (>5%) will generate an excessive amount of spinel, sacrificing mechanical strength [31].

During the process optimization, the phase diagram shows that α-Al_2O_3 is the stable phase at 1600-1700 ℃ . Combined with what was mentioned earlier, sintering at 1650 ℃ was comprehensively selected and the cooling rate was controlled to be less than 5°C per minute to avoid non-equilibrium phases (such as θ-Al_2O_3) [32]. However, there are also practical challenges in the process. The phase diagram cannot predict local component fluctuations. For instance, the issue of SiO_2 enrichment mentioned by Burhanuddin et al. in their paper requires the optimization of powder uniformity through the ball milling process .

The phase diagram also predicts the "chemical reactions" between the different phases inside the material. The first is the interface reaction. When the Al_2O_3 sheet was co-fired with the Ag-Pd electrode, the phase diagram predicts that the $MgAl_2O_4$ (spinel) interface . The thermal expansion coefficient (8.0×10^{-6}/°C) matches the Al_2O_3 (7.5×10^{-6}/°C) $_3$ [33].Therefore, electrode co-firing is not applicable to prepare Al electron substrate in production. According to the experimental verification of Kang et Al., SEM-EDX analysis shows the enrichment of Mg and Al at the interface, which is consistent with the prediction of phase diagram .

The significant main causes of early failure or damage of electronic substrate ceramics are thermal stress cracking and environmental corrosion. However, it should be noted that in the practical application of electronic substrates, the following failures or damages should not be judged only through phase diagrams, but should be judged in combination with more experimental and characterization data.

For thermal stress cracking, the phase diagram shows that the α→θ-Al_2O_3 phase transition is accompanied by volume shrinkage (5%). Early failure or damage can be judged by observing the volume shrinkage. Rapid cooling may lead to microcracks. As mentioned above, the cooling rate (<5°C/min) needs to be controlled [34].In figure 10,we can see the Al_2O_3 Surface SEM image of the coating under isothermal oxidation at different temperature.

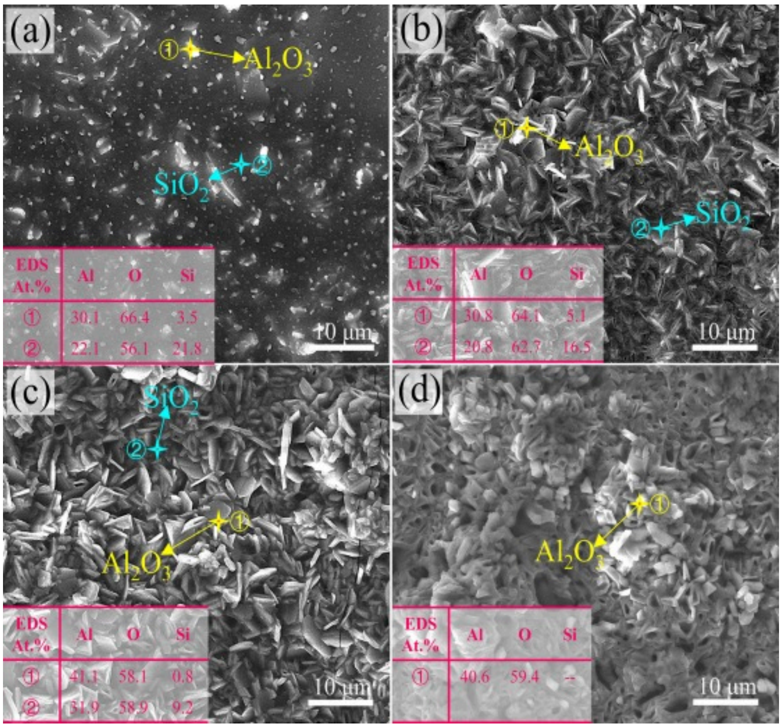

(a)

EDS At.%	Al	O	Si
①	30.1	66.4	3.5
②	22.1	56.1	21.8

(b)

EDS At.%	Al	O	Si
①	30.8	64.1	5.1
②	20.8	62.7	16.5

(c)

EDS At.%	Al	O	Si
①	41.1	58.1	0.8
②	31.9	58.9	9.2

(d)

EDS At.%	Al	O	Si
①	40.6	59.4	--

Figure 10: Al_2O_3 Surface SEM image of the coating under isothermal oxidation at 1300 °C for 0.5 h (a), 2 h (b), 4 h (c) and 6 h (d)

In a humid environment, environmental corrosion of the material may also occur, causing the SiO_2 area to absorb moisture and form a glass phase, reducing mechanical strengthWe refer to the interface area of the two phases in the phase diagram and jointly suppress the SiO_2 activity by adding a hydrophobic layer of MgO and the material. However, during the long-term high-temperature service of electronic substrates, Vollmann et al. found that the creep behavior of trace glass phases might lead to grain boundary slippage, which needs to be verified through accelerated aging experiments and cannot be determined solely through phase diagrams [35].

The phase diagram under non-equilibrium conditions has three main characteristics. First, there is the residual θ-Al_2O_3 caused by rapid cooling. Laser melting or rapid sintering can enable metastable θ-Al_2O_3 to persist, and its dielectric loss ($\tan\delta \approx 0.005$) is higher than that of the α phase. In addition to optimizing the process through phase diagrams, combining non-equilibrium phase diagrams (such as TTT curves) can enable us to quantify the relationship between the proportion of metastable phases and performance. The second point is the non-equilibrium defect. Local component fluctuations will form a trace glass phase in the SiO_2 rich region, and it is necessary to promote its crystallization through heat treatment (1050℃/2h) [36]. As mentioned above, the defect of oxygen vacancies can also be regarded as a feature. Under non-equilibrium conditions, the concentration of oxygen vacancies increases, which may cause leakage current [37]. Sintering in an oxidizing atmosphere is required to suppress the vacancies.

4. Conclusion

In this work, we have demonstrated that the performance of alumina ceramic substrates is closely linked to their crystal structure, bonding configuration, and phase stability. Through in-depth analysis of binary and ternary phase diagrams, we clarified how sintering additives and atmosphere affect the formation of α-Al_2O_3 and the suppression of undesirable phases. Optimized parameters, such as MgO content and sintering temperature, were proposed to achieve desirable mechanical and dielectric properties. These insights offer a comprehensive foundation for improving the reliability and performance of alumina-based electronic substrates in advanced applications.

References

[1] Y.G. Yushkov, E.M. Oks, A.V. Tyunkov, A.Y. Yushenko, D.B. Zolotukhin, Electron-Beam Deposition of Aluminum Nitride and Oxide Ceramic Coatings for Microelectronic Devices, Coatings 11(6) (2021).

[2] C. Zhang, L. Zuo, Z. Hu, R. Lin, H. Zhao, C. Shen, X. Cheng, Synthesis, protection performance, and failure analysis of α-Al2O3/Mo(Si, Al)2 coatings, Surface and Coatings Technology 474 (2023) 130091.

[3] Y. Hao, G. Zhang, L. Bai, Z. Yang, H. Jin, S. Gao, Interfacial microstructures and thermal/electrical conductivity of high-temperature co-fired alumina ceramic substrates, International Journal of Applied Ceramic Technology 22(3) (2024).

[4] C. Liang, Z. Li, C. Wang, K. Li, Y. Xiang, X. Jia, Laser drilling of alumina ceramic substrates: A review, Optics & Laser Technology 167 (2023).

[5] X.C. Wang, H.Y. Zheng, P.L. Chu, J.L. Tan, K.M. Teh, T. Liu, B.C.Y. Ang, G.H. Tay, Femtosecond laser drilling of alumina ceramic substrates, Applied Physics A 101(2) (2010) 271-278.

[6] S. ARAMAKI, R. ROY, Revised Phase Diagram for the System Al2O3—SiO2, Journal of the American Ceramic Society 45(5) (1962) 229-242.

[7] N. Salles, O. Politano, E. Amzallag, R. Tétot, Molecular dynamics study of high-pressure alumina polymorphs with a tight-binding variable-charge model, Computational Materials Science 111 (2016) 181-189.

[8] I. Levin, D. Brandon, Metastable Alumina Polymorphs: Crystal Structures and Transition Sequences, Journal of the American Ceramic Society 81(8) (2005) 1995-2012.

[9] Y. He, S. Liu, M. Wang, Q. Cheng, H. Ji, T. Qian, C. Yan, Advanced In Situ Characterization Techniques for Direct Observation of Gas-Involved Electrochemical Reactions, Energy & Environmental Materials 6(6) (2023).

[10] M. Sardarian, O. Mirzaee, A. Habibolahzadeh, Influence of injection temperature and pressure on the properties of alumina parts fabricated by low pressure injection molding (LPIM), Ceramics International 43(6) (2017) 4785-4793.

[11] M. Wang, F. Xie, J. Du, Z. Zhao, H. Zhang, H. Chen, B. Tang, X. Tan, Effects of crystallization of inter-granular glassy phase on the mechanical performance of alumina ceramics, Ceramics International 49(23) (2023) 39617-39626.

[12] Y. Mechiche, D. Lofficial, S. Humbert, M. Digne, A. Méthivier, Rationalization of planetary ball milling process of boehmite γ-AlOOH: Towards operating conditions dependent transition alumina phase diagram, Powder Technology 433 (2024).

[13] Y. Yuan, J. Fan, J. Li, J. Liu, K. Zhao, D. Liu, L. An, Oscillatory pressure sintering of Al2O3 ceramics, Ceramics International 46(10) (2020) 15670-15673.

[14] Y. Kang, D. Sichen, K. Morita, Activities of SiO_2 in some CaO-Al_2O_3-SiO_2(-10%MgO) melts with low SiO_2 contents at 1873K, Isij International 47(6) (2007) 805-810.

[15] D. Ghosh, V.A. Krishnamurthy, S.R. Sankaranarayanan, APPLICATION OF OPTICAL BASICITY TO VISCOSITY OF HIGH ALUMINA BLAST FURNACE SLAGS, Journal of Mining and Metallurgy Section B-Metallurgy 46(1) (2010) 41-49.

[16] Y.N. Shieh, R.R. D., D.R.F. and West, Constitution of laser melted Al2O3–MgO–SiO2 ceramics, Materials Science and Technology 11(9) (1995) 863-869.

[17] M.I. Martin, F. Andreola, L. Barbieri, F. Bondioli, I. Lancellotti, J. Ma. Rincon, M. Romero, Crystallisation and microstructure of nepheline-forsterite glass-ceramics, Ceramics International 39(3) (2013) 2955-2966.

[18] N.J. Azín, M.A. Camerucci, A.L. Cavalieri, Crystallisation of non-stoichiometric cordierite glasses, Ceramics International 31(1) (2005) 189-195.

[19] S. Michelic, J. Goriupp, S. Feichtinger, Y.-B. Kang, C. Bernhard, J. Schenk, Study on Oxide Inclusion Dissolution in Secondary Steelmaking Slags using High Temperature Confocal Scanning Laser Microscopy, Steel Research International 87(1) (2016) 57-67.

[20] Y. Yi, Y. Lin, M. Fang, W. Ma, W. Liu, Prediction Model for SiO_2 Activity in the CaO-Al_2O_3-SiO_2-MgO Quaternary Slag System, Minerals 13(4) (2023).

[21] G. Zhang, G. Cheng, Y. Huang, Y. Wang, W. Shen, H. Miao, X. Zhang, C. Yuan, Formation and Control of Large Oxide Inclusions at the Spot-Segregation Defects of Al-Killed GCr15SiMn Ingots, Metallurgical and Materials Transactions B-Process Metallurgy and Materials Processing Science 54(4) (2023) 1725-1738.

[22] Z. Tong, J. Qiao, X. Jiang, Hot Metal Desulfurization Kinetics by CaO-Al_2O_3-SiO_2-MgO-TiO_2-Na_2O Slags, Isij International 57(2) (2017) 245-253.

[23] Y. Gao, M. Leng, Y. Chen, Z. Chen, J. Li, Crystallization Products and Structural Characterization of CaO-SiO2-Based Mold Fluxes with Varying Al2O3/SiO2 Ratios, Materials 12(2) (2019) 206.

[24] Y. Kanda, K. Nakata, C. Temma, M. Sugioka, Y. Uemichi, Effects of Support on Formation of Active Sites and Hydrodesulfurization Activity of Rhodium Phosphide Catalyst, Journal of the Japan Petroleum Institute 55(2) (2012) 108-119.

[25] J. Kansy, A.S. Ahmed, J. Liebault, G. Moya, Surface concentration of defects at grain boundaries in sintered alumina determined by positron annihilation lifetime spectroscopy, Acta Physica Polonica A 100(5) (2001) 737-742.

[26] M.R. Cicconi, Z. Lu, T. Uesbeck, L. van Wuellen, D.S. Brauer, D. de Ligny, Influence of Vanadium on Optical and Mechanical Properties of Aluminosilicate Glasses, Frontiers in Materials 7 (2020).

[27] H. Burhanuddin, H. Harmuth, S. Vollmann, Quantification of Magnesia Dissolution in Silicate Melts and Diffusivity Determination Using Rotating Finger Test, Applied Sciences-Basel 12(24) (2022).

[28] J. Chen, H. Jian, L. Yehui, T. Rui, B. Chenguang, Z. Shengfu, M. and Hu, Effect of Al2O3 on the sintering process and the metallurgical performance of sinter, Canadian Metallurgical Quarterly 1-9.

[29] K. Hashimoto, K. Niwa, THE EFFECT OF MGO ADDITION ON MULLITE SUBSTRATE, Yogyo-Kyokai-Shi 95(10) (1987) 1037-1039.

[30] H.M. de Oliveira, H.d.L. Lira, L.N.d.L. Santana, Thermal Processing Effects on Biomass Ash Utilization for Ceramic Membrane Fabrication, Sustainability 17(3) (2025).

[31] F.F. Chamasemani, F. Lenzhofer, R. Brunner, Deep learning revealed statistics of the MgO particles dissolution rate in a CaO-Al_2O_3-SiO_2-MgO slag, Scientific Reports 14(1) (2024).

[32] Burhanuddin, H. Harmuth, Dissolution of Magnesia in Silicate Melts and Diffusivity Determination from CLSM Studies, Applied Sciences-Basel 13(14) (2023).

[33] Y. Ren, L. Zhang, Thermodynamic Model for Prediction of Slag-Steel-Inclusion Reactions of 304 Stainless Steels, Isij International 57(1) (2017) 68-75.

[34] S. Vollmann, J. Guarco, Burhanuddin, Experimental, analytical, and numerical quantification of the Marangoni effect in static refractory finger test, Ceramics International 50(18) (2024) 33953-33967.

[35] D. Zhang, L. Sun, H. Sun, Q. Wang, B. Wang, L. Zhu, Mineral Transition and Chemical Reactivity Evolution of a Low-Lime Calcium Aluminate Clinker with MgO and Na_2SO_4 Codopants, Acs Omega 4(8) (2019) 13594-13602.

[36] Y. Taniguchi, N. Sano, S. Seetharaman, Sulphide Capacities of CaO-Al_2O_3-SiO_2-MgO-MnO Slags in the Temperature Range 1673-1773 K, Isij International 49(2) (2009) 156-163.

[37] Z.-F. Sun, H.-L. He, P. Li, Q.-Z. Li, The spall strength and shock compressive damage of AD95 ceramics, Acta Physica Sinica 61(9) (2012).